Inorganic Chemistry

pubs.acs.org/IC Article

Revisit the E2 Domain of Amyloid Precursor Protein: Ferroxidase, Superoxide and Peroxynitrite Scavenging Activities

Andrew T. Poore, Eli C. Zuercher, Gabriel Bury, Caslyn Whitesell, Cuong C. Nguyen, Yulia N. Pushkar, and Shiliang Tian*

Cite This: *Inorg. Chem.* 2023, 62, 10780−10791 Read Online

ACCESS | Metrics & More | Article Recommendations | Supporting Information

ABSTRACT: Amyloid precursor protein (APP) is the biological precursor of β-amyloids, a known histopathological hallmark associated with Alzheimer's disease (AD). The function of APP is of great interest yet remains elusive. One of the extracellular domains of APP, the E2 domain, has been proposed to possess ferroxidase activity and affect neuronal iron homeostasis. However, contradicting evidence has been reported, and its precise role remains inconclusive. Here, we studied the Cu-binding site of the E2 domain using extended X-ray absorption fine structure (EXAFS), UV−vis, and electron paramagnetic resonance (EPR) and discovered that a new labile water ligand coordinates to the Cu(II) cofactor in addition to the four known histidines. We explored the proposed ferroxidase activity of the Cu(II)-E2 domain through reactions with ferrous iron and observed single-turnover ferrous oxidation activity with a rate up to 1.0×10^2 M^{-1} s^{-1}. Cu(I)-E2 reacted with molecular oxygen at a rate of only 5.3 M^{-1} s^{-1}, which would restrict any potential multiturnover ferroxidase activity to this slow rate and prevents observation of activity under multiturnover conditions. The positive electrostatic potential surface of the protein indicates possible reactivity with negatively charged small substrates such as superoxide radicals ($O_2^{\bullet-}$) and peroxynitrite ($ONOO^-$) that are major contributors to the oxidative stress prevalent in the extracellular environment. Our assays showed that Cu(I)-E2 can remove $O_2^{\bullet-}$ at a rate of 1.6×10^5 M^{-1} s^{-1}, which is slower than the rates of native SODs. However, the reaction between Cu(I)-E2 and $ONOO^-$ achieved a rate of 1.1×10^5 M^{-1} s^{-1}, comparable to native $ONOO^-$ scavenger peroxiredoxins (10^5−10^7 M^{-1} s^{-1}). Therefore, the E2 domain of APP can serve as an enzymatic site that may function as a ferroxidase under substrate-limiting conditions, a supplemental $O_2^{\bullet-}$ scavenger, and an $ONOO^-$ remover in the vicinity of the cellular iron efflux channel and protect neuron cells from reactive oxygen species (ROS) and reactive nitrogen species (RNS) damage.

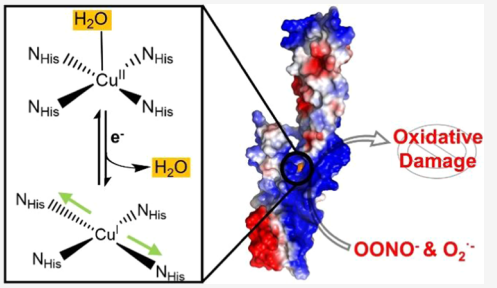

INTRODUCTION

β-Amyloid (Aβ) peptide aggregation, a type of neurotoxic senile plaques, is a main extracellular hallmark associated with Alzheimer's disease (AD).[1,2] The aggregates consist of Aβ peptides, 40 or 42 amino acid residues formed from the cleavage products of amyloid precursor protein (APP) by β- and γ-secretases through an amyloidogenic pathway (Figure 1).[3−5] Alternatively, APP can be cleaved at a different site by α-secretase through a nonamyloidogenic process, generating neuroprotective sAPPα.[5−7] Despite the extensive studies of Aβ plaques and related amyloidogenic pathways for drug discovery and medical diagnosis, the function of the upper-stream APP remains inconclusive.

APP is a transmembrane protein composed of an intracellular domain, a transmembrane helix, a juxtamembrane region, and an ectodomain (Figure 1).[8] The ectodomain contains two rigidly folded domains E1 and E2, the structures of which have been established by X-ray crystallography.[9,10] Both the E1 and E2 domains contain metal-binding sites capable of coordinating copper. The two copper binding sites in the E1 domain exhibit dissociation constants (K_d) of 0.1 and 10 nM for Cu(I) and Cu(II), respectively. On the other hand, the E2 domain features a picomolar K_d for Cu(I) and Cu(II) and includes a 4-His coordination site (Figure 1).[11] The copper sites in both domains are redox-active.[11,12]

One distinctive feature of APP is that the mRNA of the protein carries an iron response element (IRE) in its 5′ untranslated region.[13] Proteins with a 5′ IRE in their mRNAs are typically involved in either iron storage or iron efflux, and the IRE halts the protein translation under low intracellular iron conditions.[14] Besides affecting expression, iron can also impact the processing of APP by modulating the α-secretase cleavage pathway. High intracellular iron concentrations have been observed to increase sAPPα production, while low iron concentrations reduce sAPPα levels.[15] Iron accumulation in

Received: April 24, 2023
Published: June 27, 2023

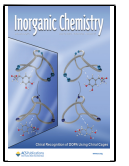

https://doi.org/10.1021/acs.inorgchem.3c01336
Inorg. Chem. 2023, 62, 10780−10791

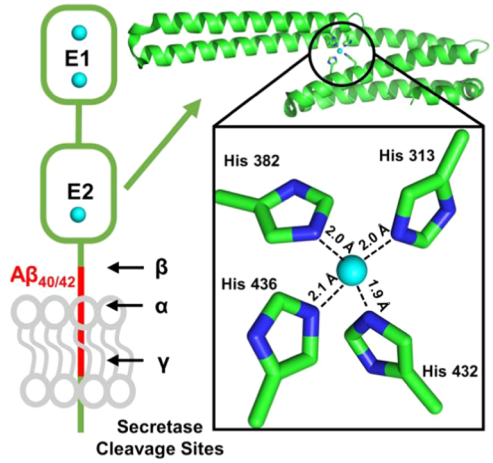

Figure 1. Left: Schematic representation of the overall structure and subdomains (E1 and E2) of APP showing cleavage sites for amyloidogenic (β and γ) and nonamyloidogenic (α) processing pathways. Right: Structure of the E2 subdomain and the zoomed-in view of the Cu-binding site (PDB: 3UMK).

the brain is a known phenomenon in neurodegenerative diseases, and a majority of AD patients have high levels of iron in various regions of the brain.[16] A positive correlation exists between brain iron accumulation and neurotoxic Aβ plaque formation.[17] These established linkages point to the possible involvement of APP in iron homeostasis, which has been a topic that has attracted dedicated research efforts.

Cellular and model animal studies have demonstrated the connection between the APP and iron homeostasis. For instance, ablation of APP695 in HEK293T cells and primary neurons induces marked iron retention, whereas increasing APP695 promotes Fe export.[18] APP knockout has been shown to alter Fe efflux in model mice, and post-translational modification of APP alters neuronal iron homeostasis.[19,20] It has been proposed that APP could bind and stabilize ferroportin (Fpn), the only known protein that exports intracellular iron in the homeostasis process.[21,22] However, fluorescence resonance energy transfer (FRET) experiments did not support the colocalization of APP and Fpn.[23] Alternatively, it has been proposed that APP functions as a ferroxidase like ceruloplasmin as part of the iron efflux process, in which the E2 domain oxidizes Fe(II) transferred from Fpn to Fe(III) before loading the Fe(III) to transferrin (Tf).[18] However, later research demonstrated that E2 domain neither binds to Fe(II) nor has ferroxidase activity.[24,25] To date, the activity of APP and its connection to iron homeostasis remain an open question.[26−28]

In this work, we studied the structure of the Cu-binding site in the E2 domain of APP by extended X-ray absorption fine structure (EXAFS) and electron paramagnetic resonance (EPR) and discovered a new labile water ligand in the first coordination sphere of Cu(II)-E2 in addition to the four known histidines. The fitting of the EXAFS data of Cu(I)-E2 suggests distortion of the four histidines and loss of the H_2O ligand upon reduction of the Cu(II) cofactor. We assayed the potential ferroxidase activity of Cu(II)-E2 using spectroscopic and kinetic methods and established the stoichiometric oxidation of Fe(II) to Fe(III) by Cu(II)-E2. We also explored the reactivities of Cu(I)-E2 with the O_2, ROS, and RNS species to evaluate the feasibility of oxidizing Cu(I)-E2 back to Cu(II)-E2 to complete the other half of the plausible catalytic cycle.

EXPERIMENTAL SECTION

General. Water was purified by using a Milli-Q IQ 7000 Lab Water System with a resistivity of 18.2 MΩ·cm.

Chemicals. GelCode blue stain reagent, GeneRuler 1 kb Plus DNA ladder, Ni-NTA (nitriloacetic acid) Superflow agarose, and glycerol were purchased from Thermo Scientific. ACS-grade copper(II) sulfate pentahydrate, α-toluenesulfonyl fluoride (PMSF), xanthine, and nitro blue tetrazolium chloride were purchased from Alfa Aesar. ACS-grade sodium chloride, sodium hydrosulfite, ACS-grade potassium phosphate dibasic anhydrous, ACS-grade potassium phosphate monobasic, ferrous ammonium sulfate hexahydrate, imidazole, tryptone yeast extract, ACS-grade dihydrate ethylenediaminetetraacetic acid disodium salt, ACS-grade L-ascorbic acid, ACS-grade sodium nitrite, 30% hydrogen peroxide, and tris base were purchased from Fisher Chemical. Xanthine oxidase from buttermilk, manganese(IV) oxide, and catalase from bovine liver were purchased from Millipore Sigma. ACS-grade sodium citrate was purchased from LabChem. 99% Extra pure sodium azide was purchased from Acros Organics.

Amyloid Precursor Protein E2 Domain Purification and Characterization. The codon-optimized gene of the E2 domain of the amyloid precursor protein (APP), residues 295−500 of APP_{695}, was synthesized and cloned into a pET-47b(+) vector using the kflI and *Bam*HI restriction sites. The construct was confirmed by Sanger sequencing. To express E2, the plasmid was transformed into *E. coli* BL21(DE3) competent cells. Cells were grown to OD_{600} = 0.8 in Terrific Broth IPTG for 4 h. The cells were harvested and lysed in the presence of PMSF, and apo-E2 was purified with a Ni-NTA column. After removal of imidazole via dialysis, the His-tag was removed by incubating with human rhinovirus (HRV) 3C protease in a 1:100 molar ratio for 4 h at 4 °C.[29] Apo-E2 was further purified with a HiPrep 16/60 Sephacryl S-100 HR size exclusion column on a BioRad NGC chromatography system. A sample of the flow-through was used for both sodium dodecyl sulfate-polyacrylamide gel electrophoresis (SDS-PAGE) and high-resolution electrospray ionization mass spectrometry (ESI-MS) analyses to confirm the purity and identity of the apo-E2 domain (Figures S6 and S7). The concentration of apo-E2 was estimated by its absorption at 280 nm with an extinction coefficient of 14,440 M^{-1} cm^{-1}.

High-Resolution ESI-MS. Purified apo or holo-E2 was exchanged into 100 mM ammonium acetate buffer pH = 7.4 via a PD-10 desalting column. Protein was then diluted with ammonium acetate buffer and concentrated to 10 μM three times to ensure complete exchange of the buffer. Formic acid was added to a final concentration of 1% v/v. All MS analyses were performed in positive-ion mode using a Thermo Finnigan LTQ orbitrap mass spectrometer equipped with a modified nanoESI source. Submicron emitters were produced from borosilicate capillary glass with filament (1.50 mm outside diameter (o.d.), 0.86 mm inner diameter (i.d.), and 10 cm length, Sutter Instruments, California) using a P-97 micropipette puller (Sutter Instruments, California), respectively. To perform nanoESI, a platinum wire was inserted into the open end of the emitter, making contact with the solution, and a voltage of ∼1.2 kV was applied. High-resolution ESI-MS spectra were deconvoluted using the UniDec software.[30]

Reconstitution of Cu(II)-E2 and Cu(I)-E2. The purified E2 domain was incubated with 1.25 mol equiv of Cu(II) sulfate pentahydrate for 1 h under stirring at 4 °C. Excess $CuSO_4$ was removed with a PD-10 desalting column. Cu(II)-E2 was either used directly or reduced to Cu(I)-E2 using 5 mol equiv of ascorbic acid in a COY Type B vinyl anaerobic chamber with oxygen content monitored by a CAM-12 monitor. The excess ascorbic acid was removed with a PD-10 desalting column. The flow-through was collected in fractions and monitored by UV−vis absorption.

HRV-3C Expression and Purification. The plasmid of HRV-3C was purchased from Addgene.[31] In brief, transformed BL21(DE3) cells were grown to OD_{600} = 0.8, induced with 0.8 mM IPTG for 4 h, and lysed via sonication. The supernatant was collected and HRV-3C was isolated via Ni-NTA. HRV-3C was further purified with a HiPrep 16/60 Sephacryl S-100 HR size exclusion column. The purified protein was stored in 10% glycerol, flash-frozen in liquid nitrogen, and stored as

https://doi.org/10.1021/acs.inorgchem.3c01336
Inorg. Chem. 2023, 62, 10780−10791

aliquots at −80 °C. An aliquot was thawed on ice immediately before use.

EPR Characterization. EPR spectra were recorded on a Bruker EMXplus EPR instrument equipped with a ColdEdge Stinger closed-cycle flow system. Cu(II)-E2 and Cu(I)-E2 samples were prepared as described above. Except when specified, the samples contained 200 μM E2 in 25 mM Tris buffer (pH = 7.4) with 150 mM NaCl. All samples were flash-frozen and stored in liquid nitrogen before analysis. EPR spectra were recorded with the following conditions: temperature 20 K, modulation amplitude 4 G, microwave power 5.0 mW, and microwave frequency ∼9.47 GHz. The EPR spectra were simulated by EasySpin.[32]

XANES and EXAFS. X-ray absorption spectra were collected at the Advanced Photon Source (APS) at Argonne National Laboratory at beamline 20-BM at a sample temperature of 20 K for the following samples: 1.06 mM Cu(II)-E2 and 1.02 mM Cu(I)-E2. To ensure minimal Cu background, a cryostat equipped with Kapton/aluminized mylar windows and exclusively employing plastic three-dimensional (3D)-printed sample holders that extend up to 10 cm above the sample was utilized. The radiation was monochromated by a Si(111) crystal. The intensity of the X-rays was monitored by three ion chambers (I_0, I_1, and I_2) filled with 50% nitrogen and 50% helium gas mixture. Copper metal foil was placed between I_2 and I_3, and its absorption was recorded with each scan for energy calibration. The energy of the first derivative peak of the Cu metal foil was calibrated to the Cu K-edge energy of 8980.3 eV. The Cu X-ray fluorescence data were collected using an X-ray fluorescence detector.

EXAFS data were analyzed using the Athena software package.[33] All data were background-corrected, normalized, and then converted to wave vector space (k-space) and weighted by k^3. k-Space data were truncated near zero crossings before the Fourier transformation. The Artemis software package was used for curve fitting. Curve fitting was done using ab initio calculated phases and amplitudes from the FEFF8 code.[34] These amplitudes and phases were used in the EXAFS equation

$$\chi(k) = S_0^2 \sum_j \frac{N_j}{kR_j^2} f_{\mathrm{eff}_j}(\pi, k, R) e^{-2\sigma_j^2 k^2} e^{-2R_j/\lambda_j(k)} \sin(2kR + \phi_{ij}(k))$$

where N_j is the number of atoms in the jth shell, R_j is the mean distance between the absorbing atom and atoms in the jth shell, and f_{eff_j} is the calculated amplitude function. The Debye−Waller term ($e^{-2\sigma_j^2 k^2}$) accounts for damping due to thermal disorder. The $e^{-2R_j/\lambda_j(k)}$ term reflects losses caused by inelastic scattering. $\lambda_j(k)$ is the electron mean free path, φ_{ij} is the calculated phase function, and S_0^2 is the amplitude reduction factor. This equation was used to fit the experimental Fourier isolated data (q-space) by using N, R, E_0, and σ^2 as variable parameters. S_0^2 was set to 1. The quality of fit was evaluated by R-factor (less than 2% denotes a good fit[35]), and the reduced χ^2 value was used to compare fits as more backscatters are included. A smaller χ^2 value implies a better fit. See Table 1for parameters of the fits.

Probing the Fifth Water Ligand with Sodium Azide. 1 μL stock solution of 1 M sodium azide in 25 mM Tris and 150 mM NaCl, pH 7.4, was added and mixed with 200 μM Cu(II)-E2 by pipetting. The UV−vis spectra were measured with an Agilent Cary-60 spectrophotometer. The titration continued until the absorption at 350 nm reached a plateau. Following titrations, 200 μL of 200 μM Cu(II)-E2 was exchanged into a buffer consisting of 25 mM Tris, 150 mM NaCl, and 1 M sodium azide at pH 7.4 and frozen for EPR analysis.

Ferroxidase Assay. Fe(II)-EDTA (ethylenediaminetetraacetic acid) and Fe(II)-citrate solutions were prepared by dissolving $(NH_4)_2Fe(SO_4)_2$ and EDTA disodium salt or sodium citrate in 1:1 ratios in H_2O and to a final concentration of 25 mM in an anaerobic chamber. This stock solution was allowed to stir for 30 min before use. Various concentrations of labile Fe(II)/Fe(II)-EDTA/Fe(II)-citrate solutions were prepared by further dilution in 25 mM Tris with 150 mM NaCl buffer at pH = 7.4. 100 μM Cu(II)-E2 and varying concentrations of ferrous sources were rapidly mixed, and full absorption spectra were anaerobically recorded by an Applied Photophysics SX.20 stopped-flow spectrometer with a PDA detector.

Table 1. EXAFS Fitting Parameters[a]

sample	shell	R, Å	N	$\sigma^2 \times 10^3$	R-factor	reduced χ^2
Cu(II)-E2 sample	Cu−N	2.02	4	5.9*	0.024	340
1.99−10.17 (k-space)	Cu−O	2.15	1	5.9*		
	Cu−C	2.57	4	10.8**		
1.2−3.9 (R-space)	Cu−C	3.04	4	10.8**		
	Cu−C	4.02	8	4.8		
Cu(I)-E2 sample	Cu−N	1.94	2	1.2	0.02	374
3.22−10.2 (k-space)	Cu−N	2.16	2	0.2		
	Cu−C	2.56	4	12.0		
0.98−4.1 (R-space)	Cu−C	2.95	4	23.5		
	Cu−C	4.09	8	13.4		

[a]Fits were done in q-space. R is the Cu-backscatter distance. σ^2 is the Debye−Waller factor. R-factor and reduced χ^2 are the goodness-of-fit parameters (see the XANES and EXAFS section). $S_o^2 = 1$ was used in all fits. * and ** denote when σ^2 was set to be the same for multiple vectors in the same coordination shell.

Cu(I)-E2 Oxidation by O_2(g). Cu(I)-E2 was prepared to a final concentration of 200 μM. 100 μL aliquot of Cu(I)-E2 was placed in a sealed anaerobic cuvette. After initial spectra were recorded for 10 s, the lid was removed and oxygen was allowed to diffuse into the system. Absorbance at 650 nm was measured. After complete oxidation of the copper center, a sample was aliquoted and saved for ESI-MS analysis. Simultaneously, a series of Cu(I)-E2 samples were exposed to oxygen and flash-frozen at various time points for EPR spectrum analysis.

Superoxide Radical Scavenging Assay. The ability of Cu(I)-E2 to reduce superoxide was assayed by a modified Fridovich method.[36,37] Superoxide was generated by a xanthine−xanthine oxidase system. The rate of superoxide generation was determined for each replicate by monitoring the nitro blue tetrazolium (NBT) reduction at 535 nm. The system contained 50 mM potassium phosphate buffer with 0.1 mM EDTA (pH = 7.8), 5×10^2 U/mL catalase solution to remove the produced peroxide, 0.1 mM NBT, and various concentrations of Cu(I)-E2. The reduction rate is defined as V_0 in the absence of Cu(I)-E2, and V in the presence of Cu(I)-E2. The reaction rate was quantified by plotting $[(V_0/V) - 1]$ against the protein concentration. The point of 50% decrease of the NBT reduction rate was defined as the concentration of protein needed for $(V_0/V) = 1 = 1$. The reaction rate was then estimated using the equation $\frac{[\mathrm{NBT}] \times k^{\mathrm{NBT}}}{[\mathrm{protein}]^{50}} = k^{\mathrm{protein}}$ with the reported reduction rate of NBT 5.94×10^4 M^{-1} s^{-1}.[36,38,39] The superoxide reduction rate by Cu(I)-E2 was measured in triplicate on three different days with freshly prepared reagents and protein. A sample from the final reaction solution was aliquoted and used for the ESI-MS analysis.

Peroxidase Assay. 200 μL of 200 μM Cu(I)-E2 solution was reacted with 0.5, 1, 2, 3, or 4 mol equiv of hydrogen peroxide at 4 °C for 30 min. A sample from the 2 mol equiv was aliquoted and used for ESI-MS analysis. The remaining solutions were flash-frozen for EPR measurement. 100 μM Cu(I)-E2 and varying concentrations of hydrogen peroxide were rapidly mixed, and full absorption spectra were anaerobically recorded by a stopped-flow spectrometer. The oxidation of Cu(I) to Cu(II) was monitored by a d−d transition centered at 650 nm.

Synthesis of Peroxynitrite. Peroxynitrite was synthesized by mixing hydrogen peroxide and nitrite under acidic conditions for 0.37 s before being quenched in basic conditions as previously described.[40] Excess hydrogen peroxide was eliminated from solution by incubation with MnO_2 for 15 min. The peroxynitrite concentration was determined spectrophotometrically at 302 nm (ε = 1700 M^{-1} cm^{-1}).[40]

Kinetic Study of the Reaction of Cu(I)-E2 with Peroxynitrite. The kinetic study for reactivity of Cu(I)-E2 with peroxynitrite was performed at room temperature as previously described for single-

https://doi.org/10.1021/acs.inorgchem.3c01336
Inorg. Chem. 2023, 62, 10780−10791

turnover assays.[41] In brief, 60, 80, 100, or 120 μM Cu(I)-E2 in 100 mM potassium phosphate buffer at pH 7.4 was mixed with 30 μM peroxynitrite dissolved in 10 mM NaOH in a 1:1 ratio. The pH after the mixture was 7.4. The reduction of peroxynitrite was monitored by decreasing absorption at 302 nm by a stopped-flow spectrometer. A minimum of 3 spectra were averaged, and the nonlinear fitting was applied to the first 400 ms to determine the reaction rate. Multiple-turnover assays were performed at room temperature by mixing 1 mM peroxynitrite measured with 2.5 mM ascorbic acid and 0, 2.5, 7.5, or 10 μM holo-E2 in 100 mM potassium phosphate buffer at pH 7.4, and the decay of peroxynitrite was monitored by the stopped-flow spectrometer. A minimum of 3 spectra were averaged. EPR samples were prepared anaerobically by consecutive additions of either 1 mM ascorbic acid or up to 240 μM peroxynitrite to 200 μM holo-E2. Additional ascorbate was removed using a PD-10 desalting column, while excess peroxynitrite was allowed to incubate and self-decay. Protein concentration was determined by taking an aliquot from the sample and measuring it via UV−vis spectroscopy. EPR intensity was concentration-corrected to 200 μM before spin quantification.

RESULTS

Spectroscopic Characterizations of Cu(II)-E2 and Cu(I)-E2. We initiated our investigation with the Cu-bound E2 domain of APP because E2 harbors a 4-His binding motif with a strong affinity for copper ions, and the domain has been proposed to have ferroxidase activity and associate with Fpn. UV−vis spectra showed that the E2 domain binds to Cu(II) quantitatively as reported with a broad d−d transition absorption centered at 650 nm (Figure S1). Continuous-wave X-band EPR characterization of the Cu(II)-E2 sample revealed $g_z > g_x \approx g_y$ and $A_z = 163 \times 10^{-4}$ cm^{-1} (Figure S2 and Table S1), suggesting a type 2 copper center with a $d_{x^2-y^2}$ ground state.[42,43] An aliquot of the Cu(II)-E2 sample was anaerobically reduced inside a glovebox with 5 mol equiv of L-ascorbate, and the excess ascorbate was removed by a PD-10 desalting column. The resulting sample was EPR-silent and lacked the d−d transition (Figures S1 and S2), suggesting the complete reduction of the Cu(II)-E2 to Cu(I)-E2.

While the solid-state structure of Cu(II)-E2 has been established by X-ray crystallography, information about the corresponding solution structure is limited. Furthermore, no structural characterization of Cu(I)-E2 has been reported. To characterize the copper coordination in E2 in solution, X-ray absorption near-edge structure (XANES) and extended X-ray absorption fine structure (EXAFS) data were collected on both Cu(II)-E2 and Cu(I)-E2 samples. For Cu(II)-E2, XANES demonstrated characteristic features for a Cu(II) center with an edge of 8992 eV (Figure 2A). The edge of Cu(I)-E2 was lowered to 8980 eV, consistent with a reduced state, which requires less energy to excite the 1s electron to the 4p orbital than that needed for an oxidized state.

The results of the EXAFS fitting and corresponding Fourier transforms are shown in Figure 2 and Tables 1 and S3. The initial values for the ligands and their distances were adopted from the Cu(II)-E2 crystal structure. EXAFS spectrum of Cu(II)-E2 displayed three peaks, corresponding to the primary Cu−N, secondary Cu−C, and tertiary Cu−N, C coordination spheres (Figure 2B). The Cu(II) distance to the four N-His was fitted to an average of 2.02 Å (Table 1), consistent with the Cu−N_{His} distances of 1.91 1.96, 2.00, and 2.06 Å reported in the crystal structure (Figure 1). The inclusion of a Cu−O distance at ∼2.1 Å resulted in improved fitting for the first peak, lowering the *R*-factor from 0.0055 to 0.004 (Table S3). This suggests the possibility of H_2O serving as a fifth ligand (vide infra). The secondary coordination sphere was disordered, as indicated by the high Debye−Waller factor. This can be attributed to the variation of the Cu−C distances in the 2.6−3.1 Å range due to the tilts of the His residues.

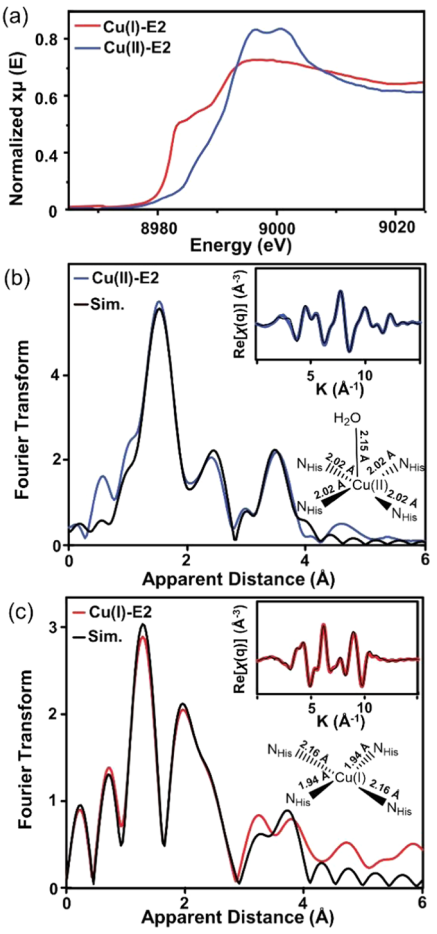

Figure 2. XANES and EXAFS Characterization of Cu(I)-E2 and Cu(II)-E2. (a) Cu K-edge XANES for Cu(I)-E2 and Cu(II)-E2. (b) EXAFS spectrum and simulation of Cu(II)-E2. (c) EXAFS spectrum and simulation of Cu(I)-E2. Insets show *q*-space filtered experimental data overlaid with fit performed in *q*-space; see the Experimental Section for details. EXAFS of Cu(II)-E2 was consistent with the reported crystal structure and demonstrated that the Cu ion is coordinated by four N-His at a distance of approximately 2.02 Å. The addition of a fifth Cu(II)−O bond at 2.15 Å, likely from coordination of a water molecule, improved the fit; see Table S3. Upon reduction to Cu(I)-E2, the EXAFS spectrum was best fitted with a Cu(I) site coordinated by four N-His and without the fifth ligand. Two N-His ligands were fitted to be 1.94 Å, and the other two were 2.16 Å from the Cu(I) center.

The reduction of the Cu(II) center significantly changed the EXAFS profile. The primary Cu−N interactions split into two sets of new scatterings at ∼1.9 and ∼2.1 Å, respectively, suggesting the distortion of the Cu site upon reduction (Figure 2C). EXAFS fitting of the Cu(I)-E2 spectrum showed that the Cu(I) center bound to two His at a closer distance of 1.94 Å and the other two His at a further distance of 2.13 Å (Figure 2C). According to the X-ray crystal structure of Cu(II)-E2 (Figure 1), the Cu ion is coordinated by four His residues that are situated within the side chains of amino acids within an inflexible α-helical structure. The Cu ion is located at the center of an α-helical bundle, and it is unlikely that the active site will deviate much from the established square planar coordination geometry upon reduction. Thus, we propose that two opposite His

https://doi.org/10.1021/acs.inorgchem.3c01336
Inorg. Chem. 2023, 62, 10780−10791

residues elongate while the other two compress in Cu(I)-E2. In Cu K-edge XAS, the shape of a feature around 8984 eV is indicative of the coordination environment of the Cu(I) site.[44] When the Cu(I) site is linear and two-coordinate, the energy of the Cu 4pz orbital is raised, leading to a low-energy 1s → $4p_{x,y}$ set of transitions at 8984 eV. However, adding a third ligand splits this degeneracy, resulting in a double-peaked spectrum. On the other hand, when the Cu(I) site is four-coordinate and approximately tetrahedral, all three 4p levels interact with the ligand field and are destabilized to higher energy. The edge of Cu(I)-E2 is inconsistent with a two-coordinate species, but it is similar to three-coordinate T-shape and four-coordinate tetrahedral species, which aligns with our current assignment of a distorted square planar geometry.

Probing the Fifth Water Ligand. The first coordination sphere of Cu(II)-E2 is comparable to that of copper-zinc superoxide dismutase (Cu,Zn-SOD) consisting of four His residues and a water molecule. The labile water in the Cu,Zn-SOD has been replaced by anions like azide, and the reaction was used to model the interaction between the enzyme and superoxide.[45,46] We employed the same approach by adding azide to the Cu(II)-E2 solution at pH 7.4 to replace the labile water and coordinate it to the Cu(II) center as the new fifth ligand. Upon addition of N_3^-, a new absorption band centered at 385 nm was observed (Figure 3A). The energy and intensity of the band were consistent with those of the ligand-to-metal charge-transfer (LMCT) N_3^- → Cu(II) band detected in Cu,Zn-SOD.[46] The dissociation constant (K_D) was determined to be 17.6 ± 6.0 mM by fitting the absorbance at 385 nm against the azide concentration (Figure 3B), and the K_D is comparable to the reported ∼11 mM K_D of Cu,Zn-SOD. The addition of N_3^- also perturbed the EPR spectrum of Cu(II)-E2, featuring a narrower hyperfine splitting with the $A_{//}$ decreasing from (163 to 149) × 10^{-4} cm^{-1} and more rhombic parameters, consistent with the presence of a stronger ligand in the axial direction (Figure 3C and Table S2). These results corroborated the existence of the fifth water ligand in Cu(II)-E2 revealed by the EXAFS spectra discussed above.

One alternative explanation would be that a His ligand is replaced by azide. The Cu ion is coordinated by four His residues that are located within the side chains of amino acids that form a rigid α-helical structure (Figure 1). Thus, the likelihood of azide replacing the His ligand is minimal. This is supported by the fact that copper ions have a picomolar affinity to the helix-rich E2 domain.[11] Furthermore, the K_d between Cu(II)-E2 and azide was determined to be around 18 mM (Figure 3), indicating weak binding that is unlikely to replace the His ligand but more probable to replace a labile water ligand.

It is worth noting that the pH-dependent change of Cu(II)-E2 EPR has been observed before by Young et al. between pH 7.4 and 9.2,[11] and the behavior was interpreted as the formation of an anionic amide ligand induced by deprotonation of the backbone peptide linkages. The pK_a of Cu-bound water is near 7.5,[47,48] while the pK_a of the peptide amide is up to 18.[49] Given the existence of the fifth water ligand revealed by the above spectroscopic studies, the observed pH-dependent EPR changes near neutral pH, but far below the peptide amide pK_a are more likely due to the deprotonation of the fifth water ligand.

Investigation of the Plausible Ferroxidase Activity of the Cu(II)-E2 Domain. The isolated E2 domain of APP was reported to oxidize Fe(II) to Fe(III).[18] However, a later study demonstrated that Cu(II)-E2 neither bound Fe(II) nor had any ferroxidase activity.[24,25] The contradicting evidence left the function of the E2 domain inconclusive. Both studies were done under multiple-turnover conditions by monitoring oxygen consumption rates in the presence of a large excess of Fe(II).[24,25] However, human ferroxidases operate under extreme substrate-limiting conditions, so the reaction kinetics are comparable to single-turnover reactions instead of typical multiturnover enzymatic reactions. We decided to first investigate whether Cu(II)-E2 could react with Fe(II) under stoichiometric conditions. Upon addition of Fe(II) to the Cu(II)-E2 solution at pH 7.4 in an anaerobic cuvette, the UV−vis spectra showed a

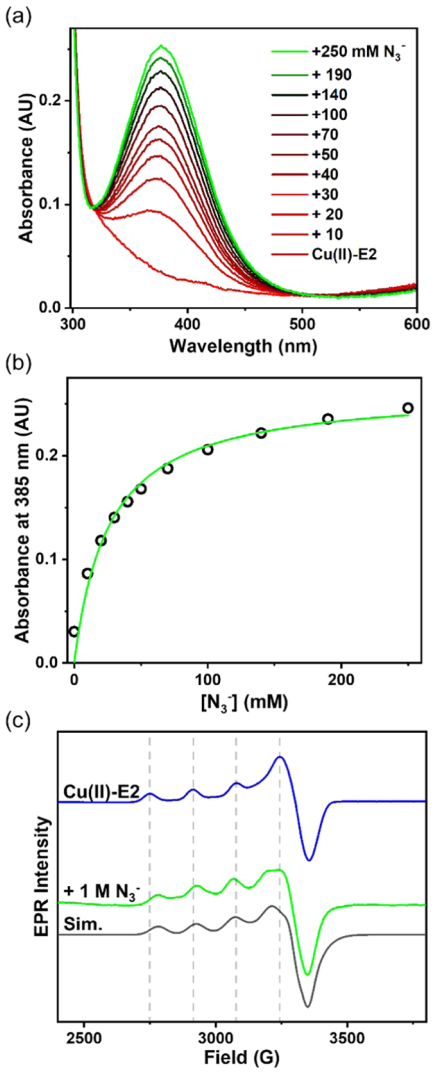

Figure 3. Probing the fifth water ligand by azide titration. (a) Absorption spectra of azide titration into 200 μM Cu(II)-E2 in 25 mM Tris pH 7.4 with 150 mM NaCl. The peak centered at 385 nm was assigned to N_3^- → Cu(II) LMCT band. (b) The dissociation constant (K_D) is determined by fitting the absorbance at 385 nm against azide concentration using the following equation: $A = A_{max} \times \{[(P + M + K_D) - (P + M + K_D)^2 - (4 \times P \times M)]^{1/2}\}/(2 \times p)$, where P = Cu(II)-E2 concentration, M = azide concentration, and K_D = dissociation constant. A dissociation constant (K_D) of 17.6 ± 6.0 mM was determined. (c) EPR spectra of 200 μM Cu(II)-E2 in 25 mM Tris, 150 mM NaCl, pH 7.4, buffer in the presence (green) or absence (blue) of 1 M azide. Conditions: temperature 20 K, modulation amplitude 4 G, microwave power 5.0 mW, and microwave frequency ∼9.47 GHz. The simulation of azide-bound Cu(II)-E2 is shown in black. Dashed gray lines represent the hyperfine splitting of Cu(II)-E2.

https://doi.org/10.1021/acs.inorgchem.3c01336
Inorg. Chem. 2023, 62, 10780−10791

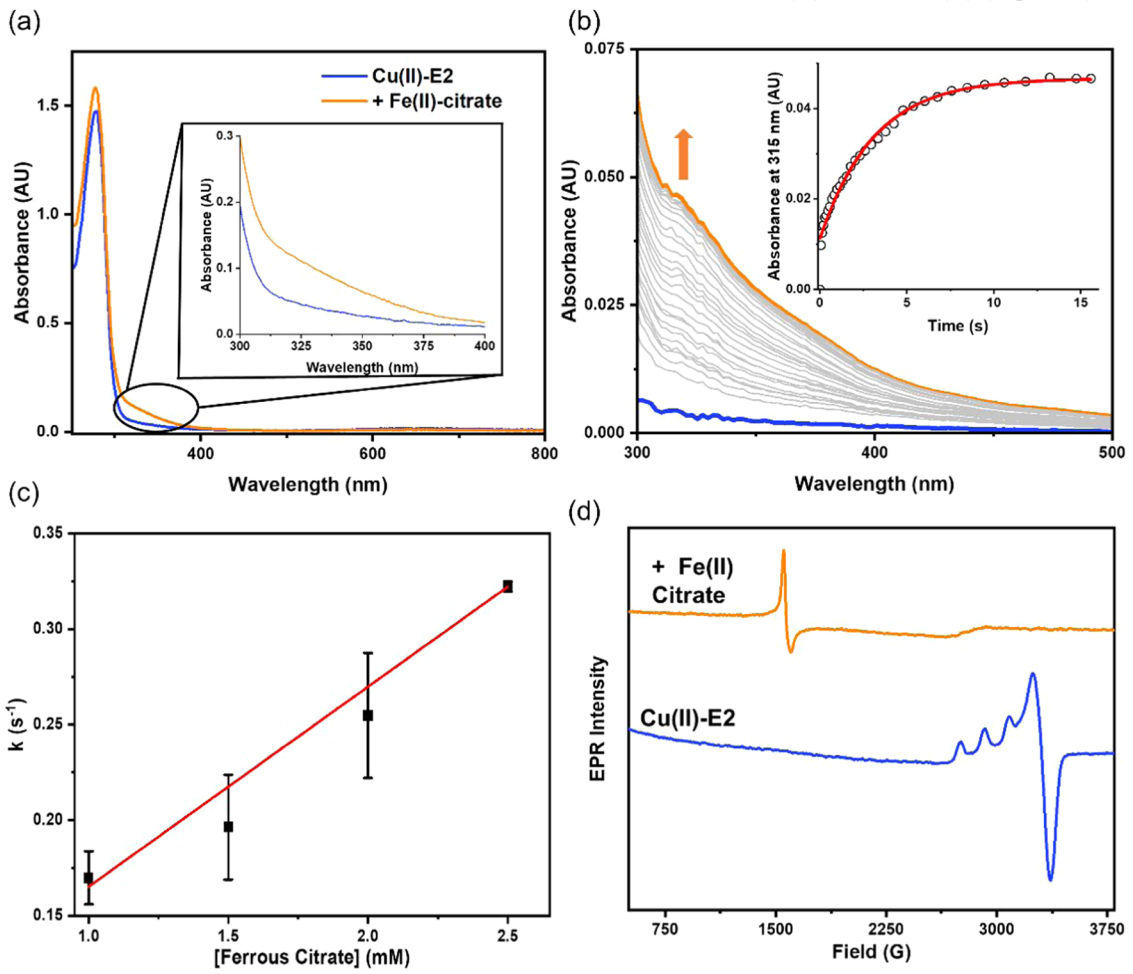

Figure 4. Ferroxidase activity of Cu(II)-E2 with Fe(II)-citrate under anaerobic conditions. (a) Absorption spectra of Cu(II)-E2 before (blue) and after (orange) the addition of Fe(II)-citrate. (b) Kinetics of Cu(II)-E2 reacting with Fe(II)-citrate. The increase at A_{315nm} as a function of reaction time is fitted with pseudo-first order. (c) Linear fitting of reaction rates to various starting Fe^{2+} concentrations gave a second-order rate constant of 1.02×10^2 between Cu(II)-E2 and Fe(II)-citrate. (d) EPR spectra of Cu(II)-E2 before (blue) and after (orange) anaerobic incubation with Fe(II)-citrate.

broad increase of absorbance centered at 315 nm, indicating the formation of Fe(III) ion (Figure S3A).[50]

We also monitored the reaction by EPR spectroscopy. Upon addition of 10 equiv of Fe(II), the EPR intensity of Cu(II)-E2 vanished, indicating the reduction of EPR-active Cu(II) to EPR-silent Cu(I) by Fe(II) (Figure S3D). Ligand-free Fe(III) is known to be labile and prone to form either ferric chloride complexes in buffered solution or precipitate out as ferric oxide, which leads to clustering and antiferromagnetic interactions of neighboring Fe(III). Therefore, no Fe(III) signal was observed in the EPR spectra, while the reduction of Cu(II)-E2 to Cu(I) by Fe(II) was observed. To determine the kinetics of the reaction between Fe(II) and Cu(II)-E2, the increase of the 315 nm absorption was monitored in the presence of various concentrations of Fe(III) (Figure S3B). By plotting the pseudo-first-order reaction rates against the starting Fe(II) concentrations, we arrived at a second-order rate constant of 3.8 M^{-1} s^{-1} between Cu(II)-E2 and Fe(II) (Figure S3C).

In biological systems, Fe(III) is usually coordinated by proteins or small molecules.[51] To explore if Cu(II)-E2 could oxidize more physiologically relevant Fe(II), we chose two chelated ferrous compounds, Fe(II)-citrate and Fe(II)-EDTA, which mimic specific Fe(II) binding sites found in ferroxidase, to react with Cu(II)-E2. Upon addition of Fe(II)-citrate or Fe(II)-EDTA to Cu(II)-E2, broad UV absorption centered around 315 nm increased in the same way as what was observed for ligand-free Fe(II) (Figures 4A and S4A). EPR measurements of the two reaction mixtures showed a similar decrease of the Cu(II) signal upon reduction of Cu(II) by the ferrous compounds. However, since citrate or EDTA as multidentate ligands can effectively coordinate to Fe(III) and prevent aggregation and the resulting antiferromagnetic interactions, the EPR signal of Fe(III)-citrate or Fe(III)-EDTA was presumed to be observable. Indeed, an increase in intensity at $g \sim 4.3$ was detected in both mixtures, demonstrating the formation of high-spin rhombic Fe(III) as expected (Figures 4D and S4D).[52] The reaction rates of Cu(II)-E2 with Fe(II)-citrate and Fe(II)-EDTA were determined to be 1.02×10^2 and 34.3 M^{-1} s^{-1} respectively (Figures 4C and S4C). As the reduction potentials of Fe(III)/Fe(II)-citrate and Fe(III)/Fe(II)-EDTA are 10 and 100 mV vs NHE at pH 7.4, respectively,[53,54] the increased driving force of the former would accelerate the electron transfer rates based on Marcus theory,[55] consistent with our observation. These stoichiometric studies demonstrated that Cu(II)-E2 is capable of oxidizing Fe(II) to Fe(III) when it reacts with labile or ligand-bound Fe(II).

Oxidation of Cu(I)-E2 by O_2 and ROS. The capability of Cu(II)-E2 to oxidize Fe(II) to Fe(III) demonstrated above supported the possibility of Cu(II)-E2 as a ferroxidase. To

https://doi.org/10.1021/acs.inorgchem.3c01336
Inorg. Chem. 2023, 62, 10780−10791

realize a catalytic cycle, the Cu(I) cofactor must be oxidized back to Cu(II) by O_2. Therefore, we assessed the reaction of Cu(I)-E2 with O_2 solubilized in a physiologically relevant buffer at pH 7.4 by spectroscopic methods.

Cu(I)-E2 was exposed to air with stirring at 20 °C, and the reaction was monitored by UV−vis spectroscopy. Absorbance centered around 650 nm arising from the d−d transition of Cu(II)-E2 was observed to increase until reaching a plateau (Figure 5A). The A_{650nm} increase was fitted with first-order reaction kinetics to yield a k_{obs} of 1.4×10^{-3} s^{-1}. Under the assumption of air saturation in the reaction system, the second-order rate constant was estimated to be 5.3 M^{-1} s^{-1}.

To corroborate the UV−vis observation and confirm the coordination sphere of the reoxidized Cu(II)-E2, the reaction was quenched at various time points and subjected to EPR measurements. As shown in Figure 5B, Cu(II)-E2 signals appeared at the 5 min time point and reached completion after 30 min. Comparison to the Cu(II)-E2 control prepared at the same concentration showed complete recovery of the Cu(II) signal at the 30 min time point, and fitting of the reference and 30 min spectra arrived at the same EPR parameters. Therefore, it can be concluded that Cu(I)-E2 could be oxidized by O_2 back to Cu(II)-E2 with the same geometry and coordinates. The concomitant one-electron reduction of O_2 to superoxide can lead to detrimental ROS.[11] However, the reduction potential of O_2/O_2^- is −0.18 V and that of O_2^-/H_2O_2 is 0.91 V. Presumably, Cu(I)-E2 could reduce superoxide to peroxide faster than reducing dioxygen to superoxide, so little ROS stress should be expected from the Cu(I)-E2 reoxidation process.

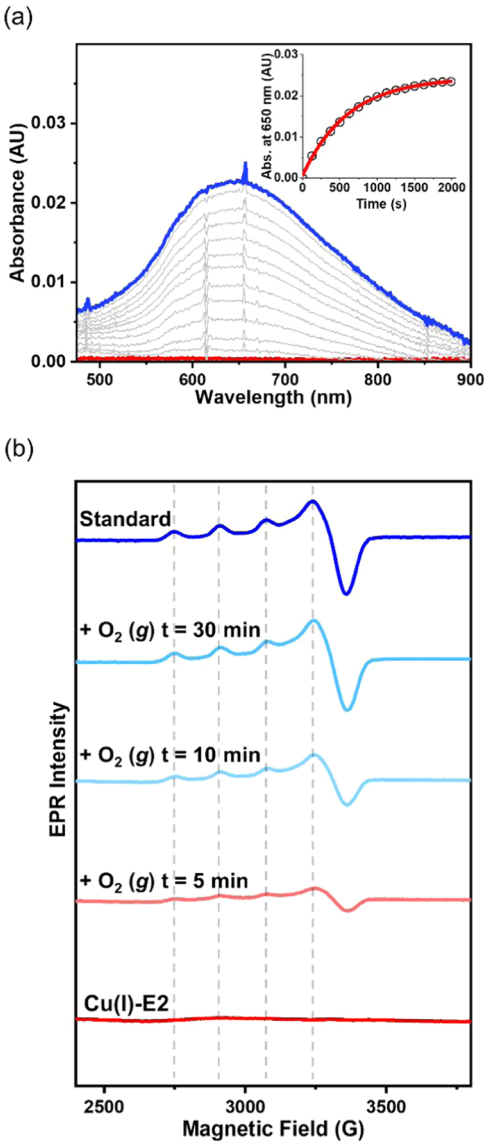

Figure 5. Oxidation of Cu(I)-E2 when exposed to O_2. (a) Cu(II)-E2 formation was monitored by the absorbance increase at 650 nm, a typical d−d transition band for Cu(II) cofactors. The increase at A_{650} was fitted with first-order reaction kinetics, and the second-order rate was determined by assuming that the O_2 concentration in the solution remained constant during the oxidation. (b) Time-dependent EPR spectra of the oxidation of Cu(I)-E2 when exposed to the air. Dashed gray lines represent the hyperfine splitting of Cu(II)-E2.

To exhaust the possible oxidation pathways of Cu(I)-E2, we further tested its reaction with superoxide and hydrogen peroxide, two ROS species that can be formed in the O_2 reduction process. The superoxide radical anion was generated in solution using a xanthine−xanthine oxidase system. We employed a competitive assay against the known superoxide scavenger nitro blue tetrazolium chloride (NBT) to determine the rate.[36] NBT reduction by superoxide leads to a characteristic band centered at 535 nm, which was monitored in the absence and presence of various concentrations of Cu(I)-E2 (Figure S5A). As expected, the initial rate of NBT reduction by superoxide decreased with increasing concentrations of Cu(I)-E2 in the reaction system (Figure S5B). Plotting the rates of NBT oxidation against the corresponding Cu(I)-E2 concentrations yielded a second-order rate constant of 1.6×10^5 M^{-1} s^{-1} for the Cu(I)-E2 oxidation by superoxide (Figure S5C), 5 orders of magnitude faster than the rate constant of Cu(I)-E2 oxidation by O_2 estimated above.

The reactivity of Cu(I)-E2 with hydrogen peroxide was evaluated similarly by mixing the holo-protein with varying concentrations of H_2O_2 in an anaerobic stopped-flow system. The recovery of Cu(II)-E2 was assessed by following the d−d transition at 650 nm (Figure S6A), and the second-order rate constant was determined to be 1.2×10^2 M^{-1} s^{-1} (Figure S6b), falling between the rate constants estimated for reactions with O_2 (5.3 M^{-1} s^{-1}) and superoxide (1.6×10^5 M^{-1} s^{-1}). EPR analyses confirmed the recovery of the Cu(II)-E2, yet only to ∼86% (Figure S6c), consistent with the slight oxidation of the protein revealed by high-resolution ESI-MS (Figure S7). The reduction of hydrogen peroxide to water requires two electrons, yet Cu(I)-E2 oxidation to Cu(II)-E2 is a one-electron process. Therefore, a highly oxidative hydroxyl radical can be generated to some extent to oxidize the protein and alter the binding pocket. Apo-E2 has been shown to dimerize,[56] so Cu(I)-E2 could also be in a dimerized format and provide the two electrons to fully reduce H_2O_2.

Oxidation of Cu(I)-E2 by Peroxynitrite. Peroxynitrite ($ONOO^-$) is formed by the diffusion-controlled reaction of nitric oxide (NO) with a superoxide radical ($O_2^{\bullet-}$).[57] Although peroxynitrite is a strong oxidant, it reacts at a relatively slow rate with most biological molecules permitting it to diffuse far on a cellular scale and contribute to the oxidative/nitrative stress in biological systems.[58] Proteins are estimated to react with peroxynitrite with a second-order rate constant at the 10^3 M^{-1} s^{-1} magnitude.[59] Since Cu(I)-E2 demonstrated ROS scavenging activity by removing superoxide at a rate of 1.6×10^5 M^{-1} s^{-1}, we also explored the reactivity of Cu(I)-E2 with peroxynitrite by mixing peroxynitrite with varying concentration of holo-protein

https://doi.org/10.1021/acs.inorgchem.3c01336
Inorg. Chem. 2023, 62, 10780−10791

in an anaerobic stopped-flow system. The reduction of peroxynitrite was monitored by decreasing the absorption at 302 nm (Figure 6a). The self-decay rate of peroxynitrite is 2

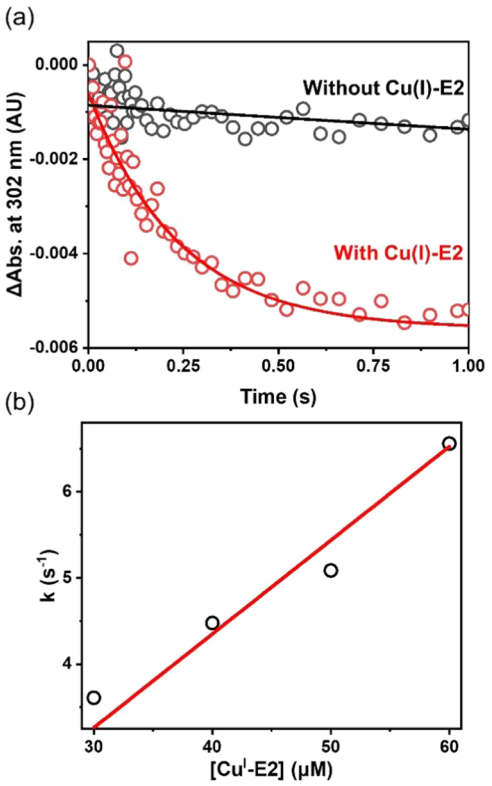

Figure 6. Oxidation of Cu(I)-E2 by peroxynitrite. (a) Reduction of peroxynitrite was monitored by the decreasing absorption at 302 nm by the stopped-flow spectrometer in the presence (red) or absence (black) of Cu(I)-E2 in 0.1 M potassium phosphate buffer, pH 7.4. A minimum of 3 spectra were averaged and the nonlinear fitting was applied to the first 400 ms to determine the reaction rate. (b) Pseudo-first-order rate constants for peroxynitrite reduction as a function of Cu(I)-E2 concentration.

orders of magnitude slower than the decay rate in the presence of Cu(I)-E2. Plotting the pseudo-first-order rate constants for peroxynitrite reduction as a function of Cu(I)-E2 concentration revealed a second-order rate constant of 1.1×10^5 M^{-1} s^{-1} (Figure 6b).

To confirm the conservation of the active site of holo-E2 upon peroxynitrite addition, Cu(II)-E2 was consecutively reduced by 5 equiv ascorbate and reoxidized by 1.2 equiv peroxynitrite three times. Excess ascorbate was removed using a PD-10 desalting column, while excess peroxynitrite was allowed to incubate and self-decay. The reaction mixture at each step was characterized by EPR (Figure 7a). Spin quantification of Cu(II) EPR intensities revealed that mixing of Cu(I)-E2 and peroxynitrite recovered 104 ± 12% of Cu(II)-E2 EPR signal without changing the hyperfine splitting (Figure 7a,7b). To test the capability of holo-E2-mediated multiple-turnover peroxynitrite reduction, the decay of peroxynitrite was measured in the presence of excess ascorbate and a catalytic amount of holo-E2 (Figure 7c). In the absence of holo-E2, peroxynitrite was reduced by ascorbate at a decay rate of 0.7 s^{-1}. In the presence of 2.5, 7.5, or 10 μM holo-E2, the decay rates of peroxynitrite increased to 1.0, 1.3, and 1.6 s^{-1}, respectively. These results demonstrated that Cu(I)-E2 is capable of performing the one-electron reduction of

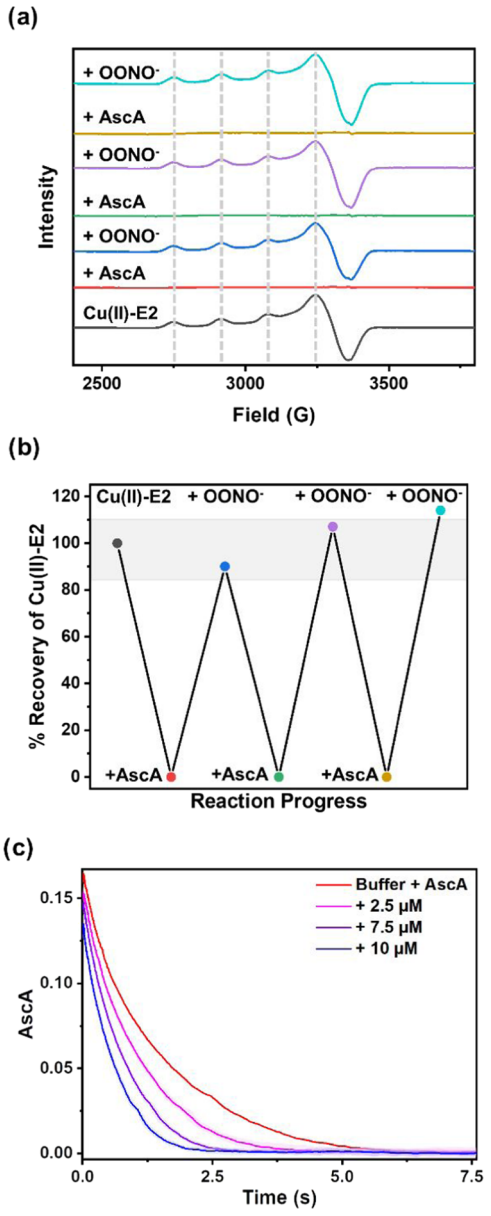

Figure 7. Multiple-turnover assays of peroxynitrite reduction mediated by holo-E2. (a) EPR spectra of holo-E2 samples prepared by consecutive additions of either 5 equiv ascorbate or up to 1.2 equiv peroxynitrite. Additional ascorbate was removed using a PD-10 desalting column while excess peroxynitrite was allowed to incubate and self-decay. (b) Spin quantification of Cu(II) EPR intensities after consecutive additions of either 5 equiv ascorbate or up to 1.5 equiv peroxynitrite. (c) Reduction of peroxynitrite monitored by the decreasing absorption at 302 nm by the stopped-flow spectrometer in the absence (red) or presence of 2.5 μM (pink), 7.5 μM (purple), or 10 μM (blue) Cu(II)-E2 in 0.1 M potassium phosphate buffer pH 7.4 containing 2.5 mM ascorbate. A minimum of 3 spectra were averaged.

peroxynitrite under multiple-turnover conditions without major changes to the electronic structure of the active site.

DISCUSSION

Copper sites in biology are involved in electron transfer, copper chaperones, or enzymatic functions. The loss of the water ligand during the redox process significantly contributes to the inner-sphere reorganization energy, which increases by ~1 eV.[60] According to the Marcus theory, an increase in reorganization

https://doi.org/10.1021/acs.inorgchem.3c01336
Inorg. Chem. 2023, 62, 10780−10791

energy is unfavorable for facile electron transfer, as most blue copper proteins have reorganization energy of 0.7 eV,[43] so the existence and dissociation of the fifth water ligand at the active site of the Cu(II)-E2 excluded electron transfer as a potential function. Copper chaperones in humans coordinate Cu(I) via 2 cysteine residues in linear geometry.[61] Native copper chaperones neither operate via 4-His coordination in square planar geometry nor are they governed by a 5′ IRE in their mRNAs. Neither geometry nor upstream genetic information on APP supports a chaperone role. On the other hand, the loss of the water ligand upon reduction is common in copper enzymes as observed in Cu,Zn-SOD and lytic polysaccharide monooxygenase.[62,63] Therefore, the observation of the fifth water ligand of Cu(II)-E2 indicates that the most possible function of Cu-E2 is enzymatic.

The E2 domain of APP is known to have high affinity for both Cu(I) and Cu(II) at the preformed 4-His binding site.[11] Our EXAFS study of the holo-protein revealed for the first time the existence of a fifth ligand, a water coordinated to the Cu(II) cofactor (Figure 2). The water could be replaced by azide similar to the axial water ligand in Cu,Zn-SOD (Figure 3),[46] which indicates that the redox-active copper site in E2 domain could not only shuffle electrons but also harbor small substrates such as ROS species. Indeed, the reactivity of the E2 domain has been an open question, and ferroxidase activity has been proposed, but with contradicting evidence. To explore the activity of E2, we evaluated the stoichiometric reaction of both ligand-free Fe(II) and two forms of chelated Fe(II) with Cu(II)-E2, and observed the formation of Fe(III) and Cu(I)-E2 in all cases. This is the first direct observation of Fe(II) oxidation by Cu(II)-E2, supporting the plausible ferroxidase activity proposed in the previous literature. Subsequent assessment of the reoxidation of Cu(I)-E2 by O_2, the other half of the plausible catalytic cycle, yielded second-order rate constants of only ~5 M^{-1} s^{-1}. Therefore, although the reaction rates between Cu(I)-E2 and O_2 are slow and consequently no multiturnover activity was observed in previous studies,[24,25] the function as ferroxidase activity still stays as a possible route under very low Fe(II) conditions.

As discussed above, SOD and E2 share a 4-His-1-H_2O structural motif in the first coordination sphere. Further analysis of the electrostatic surface of Cu(II)-E2 revealed a positive electrostatic potential surface around the substrate-access funnel (Figure 8). A similar electrostatic motif has been observed in Cu,Zn-SOD, which guides and accelerates the substrate $O_2^{\bullet-}$ into the active site.[65] Conserved Arg143 and Lys48 in Cu,Zn-SOD and Fe-SOD are 5.6 and 7.8 Å from the metal ions respectively,[45] and the two positively charged residues are known to be critical to the SOD reactivities with the negatively charged $O_2^{\bullet-}$. Comparably, a positive residue, Lys435, is located 6.3 Å from the copper site in E2. These structural features of Cu(II)-E2 indicate affinities for negatively charged substrates. Therefore, we examined the superoxide scavenging reactivity of Cu(I)-E2 and obtained a second-order rate constant of 1.6×10^5 M^{-1} s^{-1} (Figure S5). The rate is much faster than that of the reaction with O_2. However, it is slow compared to those of the native SODs (~ 10^9 M^{-1} s^{-1}),[66] so the main function of Cu(I)-E2 is possibly not as an $O_2^{\bullet-}$ scavenger. However, APP is mainly expressed in the extracellular membrane of neuron cells, where oxidative stress is prevalent. Aβ aggregates formed associated with redox-active metal ions can produce ROS that irreversibly damages cellular biomolecules and perturbs neuronal functions.[67] The superoxide scavenging activity observed in Cu-E2 can still support a supplemental role of the protein in protecting neuron cells from ROS.

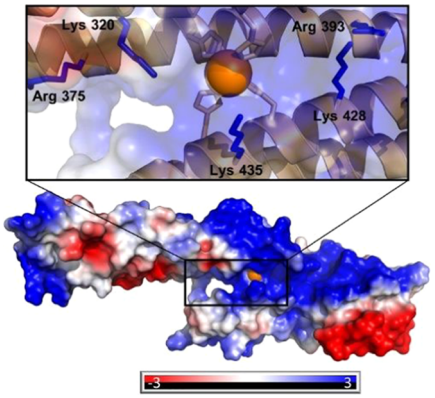

Figure 8. Predicted surface charge density map of Cu(II)-E2. The protein surface charge was estimated using APBS[64] at pH = 7.4 using the known structure of Cu(II)-E2. Positively charged side chains are shown in blue, and negatively charged side chains are shown in red. Selected positively charged amino acid side chains near the copper binding site are displayed in blue.

Peroxynitrite ($ONOO^-$) is another negatively charged small molecule that contributes to oxidative/nitrative stress in biological systems. It is a highly reactive oxidant and can react with many biological molecules like protein, DNA, and lipids. Proteins without metal cofactors have been reported to react with peroxynitrite with a rate constant of around 10^3 M^{-1} s^{-1}. Both human Mn-SOD and Cu,Zn-SOD have been shown to remove $ONOO^-$ at rates of 2.5×10^4 M^{-1} s^{-1} per monomer and 9.4×10^3 M^{-1} s^{-1}, respectively, yet Cu,Zn-SOD can be inactivated by $ONOO^-$.[68,69] We also assessed the reactivity of Cu(I)-E2 with $ONOO^-$ and obtained a second-order rate constant of 1.1×10^5 M^{-1} s^{-1} (Figure 6). Furthermore, little damage of the active site was observed after three consecutive redox cycles, supporting a multiturnover potential. $ONOO^-$ has been implicated in AD as a precursor to neuron death.[70] Nitrotyrosine, a known indicator of $ONOO^-$ stress and the product of protein nitration by $ONOO^-$, is elevated in AD patient brains compared to control brains.[70−72] The activity and robustness of Cu-E2 toward peroxynitrite and the linkage between $ONOO^-$ and AD suggest that the E2 domain of APP may function as an $ONOO^-$ scavenger in vivo. It is worth noting that peroxiredoxins (Prxs) are a family of peroxidase enzymes that rely on cysteine for their catalytic activity and play a crucial role in regulating peroxide levels within cells. Prxs are capable of catalytically reducing $ONOO^-$. Cu(I)-E2 reduces $ONOO^-$ at a rate of 10^5 M^{-1} s^{-1}, which is comparable to Prx1 and Prx2, but 2 orders of magnitude slower than Prx 5 and Prx3, which are expressed exclusively in mitochondria.[73,74] It is not uncommon for organisms to have multiple versions of enzymes that serve the same function. For example, humans have both Cu,Zn-SOD and Mn-SOD, which catalyze the dismutation of the superoxide radical, and ceruloplasmin and hephaestin, which have ferroxidase activity. Interestingly, these enzymes are located in different parts of the cell and the body. Cu,Zn-SOD is in the cytoplasm, Mn-SOD is in the mitochondria,[75] ceruloplasmin is in the serum, and hephaestin is in the intestinal enterocytes.[44] It is possible that humans have two peroxynitrite scavenging enzymes, with one located in the cytoplasm (peroxiredoxins) and the other on the membrane (E2 domain of APP).

https://doi.org/10.1021/acs.inorgchem.3c01336
Inorg. Chem. 2023, 62, 10780−10791

CONCLUSIONS

In summary, we revised the structure of Cu(II)-E2 using EXAFS to include the coordination of copper to a previously unknown fifth water ligand. Additionally, the EXAFS study also provides the first known structural information for the coordination sphere of reduced Cu(I)-E2. We evaluated the stoichiometric reaction of both ligand-free Fe(II) and two forms of chelated Fe(II) with Cu(II)-E2, and we observed the formation of Fe(III) and Cu(I)-E2 in all cases. Subsequent assessment of the reoxidation of Cu(I)-E2 by O_2, the other half of the plausible catalytic cycle, yielded a second-order rate constant of ~5 M^{-1} s^{-1}, suggesting that each step of the plausible catalytic cycle of a ferroxidase could be executed stoichiometrically, but the slow rate prevents the observation of activity under normal enzymatic multiturnover conditions. but hardly physiologically relevant. The existence of the fifth water ligand in the first coordination sphere of Cu(II)-E2 and positive electrostatic protein surface indicate potential reactivity with small anionic substrates like $O_2^{\bullet-}$ and $ONOO^-$ that are contributors to the oxidative stress prevalent in the extracellular environment. Cu(I)-E2 can remove the aqueous $O_2^{\bullet-}$ at a rate of 1.6×10^5 M^{-1} s^{-1}, which is slower than the rates of native SODs. The reaction with $ONOO^-$ yielded a rate of 1.1×10^5 M^{-1} s^{-1}, faster than those of the SODs, and the protein can withstand multiple redox cycles with peroxynitrite without active site damage. Together, the experimental evidence confirms that the E2 domain can oxidase Fe(II) to Fe(III) directly and has the potential to be a ferroxidase under extremely substrate-limiting conditions. It could function as a superoxide scavenger probably as a supplement to the native SOD system and, more importantly, can function as an $ONOO^-$ scavenger and protect neuron cells from ROS/RNS damage.

ASSOCIATED CONTENT

Supporting Information

The Supporting Information is available free of charge at: https://pubs.acs.org/doi/10.1021/acs.inorgchem.3c01336.

Spectroscopic investigation of holo-E2 (Figures S1 and S2), additional ferroxidase activity of Cu(II)-E2 (Figures S3 and S4), superoxide and peroxidase activity of Cu(I)-E2 (Figures S5 and S6), ESI-MS and SDS-PAGE gel electrophoresis data of E2 (Figures S7 and S8), and EPR and EXAFS fitting parameters of holo-E2 (Tables S1 and S3) (PDF)

AUTHOR INFORMATION

Corresponding Author

Shiliang Tian − *Department of Chemistry, Purdue University, West Lafayette, Indiana 47906, United States;* orcid.org/0000-0002-9830-5480; Email: sltian@purdue.edu

Authors

Andrew T. Poore − *Department of Chemistry, Purdue University, West Lafayette, Indiana 47906, United States*

Eli C. Zuercher − *Department of Chemistry, Purdue University, West Lafayette, Indiana 47906, United States*

Gabriel Bury − *Department of Physics and Astronomy, Purdue University, West Lafayette, Indiana 47907, United States*

Caslyn Whitesell − *Department of Chemistry, Purdue University, West Lafayette, Indiana 47906, United States*

Cuong C. Nguyen − *Department of Chemistry, Purdue University, West Lafayette, Indiana 47906, United States*

Yulia N. Pushkar − *Department of Physics and Astronomy, Purdue University, West Lafayette, Indiana 47907, United States;* orcid.org/0000-0001-7949-6472

Complete contact information is available at: https://pubs.acs.org/10.1021/acs.inorgchem.3c01336

Notes

The authors declare no competing financial interest.

ACKNOWLEDGMENTS

The authors acknowledge the support of Purdue University's Research Instrumentation Center and Na Gou in the acquisition and analysis of mass spectrometry data. Access to EPR was provided by the Amy Instrumentation Facility, Department of Chemistry, under the supervision of Dr. Michael Everly. This research was supported by NSF, CHE- 2004147 (Y.P.) and by GM132024 (T32 Molecular Biophysics Training Program to G.B.) from the National Institute of General Medical Sciences (NIGMS). The use of the Advanced Photon Source, an Office of Science User Facility operated by the U.S. Department of Energy (DOE) Office of Science by Argonne National Laboratory, was supported by the U.S. DOE under Contract DE-AC02-06CH11357. The PNC/XSD (Sector 20) facilities at the Advanced Photon Source and research at these facilities were supported by the U.S. Department of Energy, Basic Energy Science and the Canadian Light Source.

REFERENCES

(1) Alzheimer's Association. *Alzheimer's Disease Facts and Figures*, 2021; Vol. 3.

(2) Goedert, M.; Spillantini, M. G. A Century of Alzheimer's Disease. *Science* **2006**, *314* (5800), 777−781.

(3) Blennow, K.; de Leon, M. J.; Zetterberg, H. Alzheimer's disease. *Lancet* **2006**, *368* (9533), 387−403.

(4) Mattson, M. P. Pathways towards and away from Alzheimer's disease. *Nature* **2004**, *430* (7000), 631−639.

(5) Spies, P. E.; Verbeek, M. M.; van Groen, T.; Claassen, J. A. H. R. Reviewing reasons for the decreased CSF Abeta42 concentration in Alzheimer disease. *Front. Biosci.* **2012**, *17* (6), 2024−2034.

(6) Pimplikar, S. W.; Ghosal, K. Amyloid precursor protein: more than just neurodegeneration. *Stem Cell Res. Ther.* **2011**, *2* (5), No. 39.

(7) Plummer, S.; Van den Heuvel, C.; Thornton, E.; Corrigan, F.; Cappai, R. The Neuroprotective Properties of the Amyloid Precursor Protein Following Traumatic Brain Injury. *Aging Dis.* **2016**, *7* (2), 163−179.

(8) Coburger, I.; Dahms, S. O.; Roeser, D.; Gührs, K.-H.; Hortschansky, P.; Than, M. E. Analysis of the Overall Structure of the Multi-Domain Amyloid Precursor Protein (APP). *PLoS One* **2013**, *8* (12), No. e81926.

(9) Dahms, S. O.; Hoefgen, S.; Roeser, D.; Schlott, B.; Gührs, K.-H.; Than, M. E. Structure and biochemical analysis of the heparin-induced E1 dimer of the amyloid precursor protein. *Proc. Natl. Acad. Sci. U.S.A.* **2010**, *107* (12), 5381−5386.

(10) Dahms, S. O.; Könnig, I.; Roeser, D.; Gührs, K.-H.; Mayer, M. C.; Kaden, D.; Multhaup, G.; Than, M. E. Metal Binding Dictates Conformation and Function of the Amyloid Precursor Protein (APP) E2 Domain. *J. Mol. Biol.* **2012**, *416* (3), 438−452.

(11) Young, T. R.; Pukala, T. L.; Cappai, R.; Wedd, A. G.; Xiao, Z. The Human Amyloid Precursor Protein Binds Copper Ions Dominated by a Picomolar-Affinity Site in the Helix-Rich E2 Domain. *Biochemistry* **2018**, *57* (28), 4165−4176.

(12) Hureau, C. Coordination of redox active metal ions to the amyloid precursor protein and to amyloid-β peptides involved in Alzheimer disease. Part 1: An overview. *Coord. Chem. Rev.* **2012**, *256* (19−20), 2164−2174.

(13) Zhou, Z. D.; Tan, E.-K. Iron regulatory protein (IRP)-iron responsive element (IRE) signaling pathway in human neurodegenerative diseases. *Mol. Neurodegener.* **2017**, *12* (1), No. 75.
(14) Eisenstein, R. S. Iron Regulatory Proteins and the Molecular Control of Mammalian Iron Metabolism. *Annu. Rev. Nutr.* **2000**, *20* (1), 627−662.
(15) Bodovitz, S.; Falduto, M. T.; Frail, D. E.; Klein, W. L. Iron Levels Modulate α-Secretase Cleavage of Amyloid Precursor Protein. *J. Neurochem.* **2002**, *64* (1), 307−315.
(16) Belaidi, A. A.; Bush, A. I. Iron neurochemistry in Alzheimer's disease and Parkinson's disease: targets for therapeutics. *J. Neurochem.* **2016**, *139*, 179−197.
(17) Ward, R. J.; Zucca, F. A.; Duyn, J. H.; Crichton, R. R.; Zecca, L. The role of iron in brain ageing and neurodegenerative disorders. *Lancet Neurol.* **2014**, *13* (10), 1045−1060.
(18) Duce, J. A.; Tsatsanis, A.; Cater, M. A.; James, S. A.; Robb, E.; Wikhe, K.; Leong, S. L.; Perez, K.; Johanssen, T.; Greenough, M. A.; Cho, H.; Galatis, D.; Moir, R. D.; Masters, C. L.; McLean, C.; Tanzi, R. E.; Cappi, R.; Barnham, K. J.; Ciccotosto, G. D.; Rogers, J. T.; Bush, A. I. Iron-Export Ferroxidase Activity of β-Amyloid Precursor Protein Is Inhibited by Zinc in Alzheimer's Disease. *Cell* **2010**, *142* (6), 857−867.
(19) Belaidi, A. A.; Gunn, A. P.; Wong, B. X.; Ayton, S.; Appukuttan, A. T.; Roberts, B. R.; Duce, J. A.; Bush, A. I. Marked Age-Related Changes in Brain Iron Homeostasis in Amyloid Protein Precursor Knockout Mice. *Neurotherapeutics* **2018**, *15* (4), 1055−1062.
(20) Tsatsanis, A.; Dickens, S.; Kwok, J. C. F.; Wong, B. X.; Duce, J. A. Post Translational Modulation of β-Amyloid Precursor Protein Trafficking to the Cell Surface Alters Neuronal Iron Homeostasis. *Neurochem. Res.* **2019**, *44* (6), 1367−1374.
(21) McCarthy, R. C.; Park, Y.-H.; Kosman, D. J. sAPP modulates iron efflux from brain microvascular endothelial cells by stabilizing the ferrous iron exporter ferroportin. *EMBO Rep.* **2014**, *15* (7), 809−815.
(22) Wong, B. X.; Tsatsanis, A.; Lim, L. Q.; Adlard, P. A.; Bush, A. I.; Duce, J. A. β-Amyloid Precursor Protein Does Not Possess Ferroxidase Activity but Does Stabilize the Cell Surface Ferrous Iron Exporter Ferroportin. *PLoS One* **2014**, *9* (12), No. e114174.
(23) Dlouhy, A. C.; Bailey, D. K.; Steimle, B. L.; Parker, H. V.; Kosman, D. J. Fluorescence resonance energy transfer links membrane ferroportin, hephaestin but not ferroportin, amyloid precursor protein complex with iron efflux. *J. Biol. Chem.* **2019**, *294* (11), 4202−4214.
(24) Ebrahimi, K. H. H.; Hagen, P. L.; Hagen, W. R. A Synthetic Peptide with the Putative Iron Binding Motif of Amyloid Precursor Protein (APP) Does Not Catalytically Oxidize Iron. *PLoS One* **2012**, *7* (8), No. e40287.
(25) Ebrahimi, K. H.; Dienemann, C.; Hoefgen, S.; Than, M. E.; Hagedoorn, P. L.; Hagen, W. R. The Amyloid Precursor Protein (APP) Does Not Have a Ferroxidase Site in Its E2 Domain. *PLoS One* **2013**, *8* (8), No. e72177.
(26) Lahiri, D. K.; Maloney, B.; Wang, R. APPealing for a role in cellular iron efflux. *J. Biol. Chem.* **2019**, *294* (24), 9365.
(27) Kosman, D. J. Reply to Lahiri et al.: APPealing for a role in cellular iron efflux. *J. Biol. Chem.* **2019**, *294* (24), 9366.
(28) Bailey, D. K.; Kosman, D. J. Is brain iron trafficking part of the physiology of the amyloid precursor protein. *J. Biol. Inorg. Chem.* **2019**, *24* (8), 1171−1177.
(29) Abdelkader, E. H.; Otting, G. NT*-HRV3CP: An optimized construct of human rhinovirus 14 3C protease for high-yield expression and fast affinity-tag cleavage. *J. Biotechnol.* **2021**, *325*, 145−151.
(30) Marty, M. T.; Baldwin, A. J.; Marklund, E. G.; Hochberg, G. K. A.; Benesch, J. L. P.; Robinson, C. V. Bayesian Deconvolution of Mass and Ion Mobility Spectra: From Binary Interactions to Polydisperse Ensembles. *Anal. Chem.* **2015**, *87* (8), 4370−4376.
(31) Raran-Kurussi, S.; Waugh, D. S. A dual protease approach for expression and affinity purification of recombinant proteins. *Anal. Biochem.* **2016**, *504*, 30−37.
(32) Stoll, S.; Schweiger, A. EasySpin, a comprehensive software package for spectral simulation and analysis in EPR. *J. Magn. Reson.* **2006**, *178* (1), 42−55.
(33) Ravel, B.; Newville, M. ATHENA, ARTEMIS, HEPHAESTUS: data analysis for X-ray absorption spectroscopy using IFEFFIT. *J. Synchrotron Radiat.* **2005**, *12* (4), 537−541.
(34) Rehr, J. J.; Albers, R. C. Theoretical approaches to x-ray absorption fine structure. *Rev. Mod. Phys.* **2000**, *72* (3), 621−654.
(35) Koningsberger, D. C.; Prins, R. *X-ray Absorption: Principles, Applications, Techniques of EXAFS, SEXAFS, and XANES*; John Wiley and Sons: New York, NY, 1988.
(36) Liu, J.; Meier, K. K.; Tian, S.; Zhang, J.-l.; Guo, H.; Schulz, C. E.; Robinson, H.; Nilges, M. J.; Münck, E.; Lu, Y. Redesigning the Blue Copper Azurin into a Redox-Active Mononuclear Nonheme Iron Protein: Preparation and Study of Fe(II)-M121E Azurin. *J. Am. Chem. Soc.* **2014**, *136* (35), 12337−12344.
(37) Beauchamp, C.; Fridovich, I. Superoxide dismutase: Improved assays and an assay applicable to acrylamide gels. *Anal. Biochem.* **1971**, *44* (1), 276−287.
(38) Liao, Z.-R.; Zheng, X.-F.; Luo, B.-S.; Shen, L.-R.; Li, D.-F.; Liu, H.-L.; Zhao, W. Synthesis, characterization and SOD-like activities of manganese-containing complexes with N,N,N′,N′-tetrakis(2′-benzimidazolyl methyl)-1,2-ethanediamine (EDTB). *Polyhedron* **2001**, *20* (22−23), 2813−2821.
(39) Bielski, B. H. J.; Richter, H. W. A study of the superoxide radical chemistry by stopped-flow radiolysis and radiation induced oxygen consumption. *J. Am. Chem. Soc.* **1977**, *99* (9), 3019−3023.
(40) Robinson, K. M.; Beckman, J. Synthesis of Peroxynitrite from Nitrite and Hydrogen Peroxide. In *Methods in Enzymology*; Elsevier, 2005; Vol. *396*, pp 207−214.
(41) Briviba, K.; Kissner, R.; Koppenol, W. H.; Sies, H. Kinetic Study of the Reaction of Glutathione Peroxidase with Peroxynitrite. *Chem. Res. Toxicol.* **1998**, *11* (12), 1398−1401.
(42) Solomon, E. I.; Baldwin, M. J.; Lowery, M. D. Electronic structures of active sites in copper proteins: contributions to reactivity. *Chem. Rev.* **1992**, *92* (4), 521−542.
(43) Gray, H. B.; Malmström, B. G.; Williams, R. J. P. Copper coordination in blue proteins. *J. Biol. Inorg. Chem.* **2000**, *5* (5), 551−559.
(44) Solomon, E. I.; Heppner, D. E.; Johnston, E. M.; Ginsbach, J. W.; Cirera, J.; Qayyum, M.; Kieber-Emmons, M. T.; Kjaergaard, C. H.; Hadt, R. G.; Tian, L. Copper Active Sites in Biology. *Chem. Rev.* **2014**, *114* (7), 3659−3853.
(45) Sheng, Y.; Abreu, I. A.; Cabelli, D. E.; Maroney, M. J.; Miller, A.-F.; Teixeira, M.; Valentine, J. S. Superoxide Dismutases and Superoxide Reductases. *Chem. Rev.* **2014**, *114* (7), 3854−3918.
(46) Dooley, D. M.; McGuirl, M. A. Thermodynamics of azide and thiocyanate binding to bovine copper-zinc superoxide dismutase. *Inorg. Chem.* **1986**, *25* (8), 1261−1264.
(47) Huheey, J. E. *Inorganic Chemistry: Principles of Structure and Reactivity*; Harper & Row, 1983.
(48) Burgess, J. *Metal Ions in Solution*; Ellis Horwood, 1978.
(49) Eriksson, M. A.; Härd, T.; Nilsson, L. On the pH dependence of amide proton exchange rates in proteins. *Biophys. J.* **1995**, *69* (2), 329−339.
(50) Bonomi, F.; Kurtz, D. M.; Cui, X. Ferroxidase activity of recombinant Desulfovibrio vulgaris rubrerythrin. *J. Biol. Inorg. Chem* **1996**, *1* (1), 67−72.
(51) Grass, G. Iron Transport in Escherichia Coli: All has not been said and Done. *BioMetals* **2006**, *19* (2), 159−172.
(52) Bou-Abdallah, F.; Chasteen, N. D. Spin concentration measurements of high-spin (g′ = 4.3) rhombic iron(III) ions in biological samples: theory and application. *J. Biol. Inorg. Chem.* **2007**, *13* (1), 15−24.
(53) Adam, F. I.; Bounds, P. L.; Kissner, R.; Koppenol, W. H. Redox Properties and Activity of Iron−Citrate Complexes: Evidence for Redox Cycling. *Chem. Res. Toxicol.* **2015**, *28* (4), 604−614.
(54) Shimizu, K.; Hutcheson, R.; Engelmann, M. D.; Cheng, I. F. Cyclic voltammetric and aqueous equilibria model study of the pH dependent iron(II/III)ethylenediamminetetraacetate complex reduction potential. *J. Electroanal. Chem.* **2007**, *603* (1), 44−50.

https://doi.org/10.1021/acs.inorgchem.3c01336
Inorg. Chem. 2023, 62, 10780−10791

(55) Marcus, R. A.; Sutin, N. Electron transfers in chemistry and biology. *Biochim. Biophys. Acta, Rev. Bioenerg.* **1985**, *811* (3), 265−322.
(56) Lee, S.; Xue, Y.; Hu, J.; Wang, Y.; Liu, X.; Demeler, B.; Ha, Y. The E2 Domains of APP and APLP1 Share a Conserved Mode of Dimerization. *Biochemistry* **2011**, *50* (24), 5453−5464.
(57) Szabó, C.; Ischiropoulos, H.; Radi, R. Peroxynitrite: biochemistry, pathophysiology and development of therapeutics. *Nat. Rev. Drug Discovery* **2007**, *6* (8), 662−680.
(58) Pacher, P.; Beckman, J.; Liaudet, L. Nitric Oxide and Peroxynitrite in Health and Disease. *Physiol. Rev.* **2007**, *87*, 315−424.
(59) Alvarez, B.; Ferrer-Sueta, G.; Freeman, B. A.; Radi, R. Kinetics of Peroxynitrite Reaction with Amino Acids and Human Serum Albumin. *J. Biol. Chem.* **1999**, *274* (2), 842−848.
(60) Basumallick, L.; Sarangi, R.; DeBeer George, S.; Elmore, B.; Hooper, A. B.; Hedman, B.; Hodgson, K. O.; Solomon, E. I. Spectroscopic and Density Functional Studies of the Red Copper Site in Nitrosocyanin: Role of the Protein in Determining Active Site Geometric and Electronic Structure. *J. Am. Chem. Soc.* **2005**, *127* (10), 3531−3544.
(61) Fukai, T.; Ushio-Fukai, M.; Kaplan, J. H. Copper transporters and copper chaperones: roles in cardiovascular physiology and disease. American journal of physiology. *Cell Physiol.* **2018**, *315* (2), C186−C201.
(62) Hough, M. A.; Hasnain, S. S. Structure of Fully Reduced Bovine Copper Zinc Superoxide Dismutase at 1.15 Å. *Structure* **2003**, *11* (8), 937−946.
(63) Tandrup, T.; Muderspach, S. J.; Banerjee, S.; Santoni, G.; Ipsen, J.; Hernández-Rollán, C.; Nørholm, M. H. H.; Johansen, K. S.; Meilleur, F.; Lo Leggio, L. Changes in active-site geometry on X-ray photoreduction of a lytic polysaccharide monooxygenase active-site copper and saccharide binding. *IUCrJ* **2022**, *9* (Pt5), 666−681.
(64) Jurrus, E.; Engel, D.; Star, K.; Monson, K.; Brandi, J.; Felberg, L. E.; Brookes, D. H.; Wilson, L.; Chen, J.; Liles, K.; Chun, M.; Li, P.; Gohara, D. W.; Dolinsky, T.; Konecny, R.; Koes, D. R.; Nielsen, J. E.; Head-Gordon, T.; Geng, W.; Krasny, R.; Wei, G. W.; Holst, M. J.; McCammon, J. A.; Baker, N. A. Improvements to the APBS biomolecular solvation software suite. *Protein Sci.* **2018**, *27* (1), 112−128.
(65) Perry, J. J. P.; Shin, D. S.; Getzoff, E. D.; Tainer, J. A. The structural biochemistry of the superoxide dismutases. *Biochim. Biophys. Acta, Proteins Proteomics* **2010**, *1804* (2), 245−262.
(66) Antonyuk, S. V.; Strange, R.; Marklund; Hasnain, S. The Structure of Human Extracellular Copper−Zinc Superoxide Dismutase at 1.7 Å Resolution: Insights into Heparin and Collagen Binding. *J. Mol. Biol.* **2009**, *388* (2), 310−326.
(67) Cheignon, C.; Tomas, M.; Bonnefont-Rousselot, D.; Faller, P.; Hureau, C.; Collin, F. Oxidative stress and the amyloid beta peptide in Alzheimer's disease. *Redox. Biol.* **2018**, *14*, 450−464.
(68) Alvarez, B.; Demicheli, V.; Durán, R.; Trujillo, M.; Cerveñansky, C.; Freeman, B.; Radi, R. Inactivation of human Cu,Zn superoxide dismutase by peroxynitrite and formation of histidinyl radical. *Free Radical Biol. Med.* **2004**, *37* (6), 813−822.
(69) Quijano, C.; Hernandez-Saavedra, D.; Castro, L.; McCord, J. M.; Freeman, B. A.; Radi, R. Reaction of Peroxynitrite with Mn-Superoxide Dismutase. *J. Biol. Chem.* **2001**, *276* (15), 11631−11638.
(70) Torreilles, F.; Salman-Tabcheh, S.; Guérin, M. G.; J, T. Neurodegenerative disorders: the role of peroxynitrite. *Brain Res. Rev.* **1999**, *30* (2), 153−163.
(71) Smith, M. A.; Richey Harris, P. L.; Sayre, L. M.; Beckman, J. S.; Perry, G. Widespread Peroxynitrite-Mediated Damage in Alzheimer's Disease. *J. Neurosci.* **1997**, *17* (8), 2653−2657.
(72) Zhang, Y.-J.; Xu, Y.-F.; Liu, Y.-H.; Yin, J.; Li, H.-L.; Wang, Q.; Wang, J.-Z. Peroxynitrite induces Alzheimer-like tau modifications and accumulation in rat brain and its underlying mechanisms. *FASEB J.* **2006**, *20* (9), 1431−1442.
(73) Trujillo, M.; Ferrer-Sueta, G.; Thomson, L.; Flohé, L.; Radi, R. Kinetics of Peroxiredoxins and their Role in the Decomposition of Peroxynitrite. *Subcell. Biochem.* **2007**, *44*, 83−113.
(74) De Armas, M. I.; Esteves, R.; Viera, N.; Reyes, A. M.; Mastrogiovanni, M.; Alegria, T. G. P.; Netto, L. E. S.; Tórtora, V.; Radi, R.; Trujillo, M. Rapid peroxynitrite reduction by human peroxiredoxin 3: Implications for the fate of oxidants in mitochondria. *Free Radical Biol. Med.* **2019**, *130*, 369−378.
(75) Fukai, T.; Ushio-Fukai, M. Superoxide Dismutases: Role in Redox Signaling, Vascular Function, and Diseases. *Antioxid. Redox Signaling* **2011**, *15* (6), 1583−1606.

https://doi.org/10.1021/acs.inorgchem.3c01336
Inorg. Chem. 2023, 62, 10780−10791